Reduced-order models for the analysis of a vertical rod under parametric excitation

note finali coverpage

(Article begins on next page)

15 May 2024

# Reduced-order models for the analysis of a vertical rod under parametric excitation

Guilherme Jorge Vernizzi[a,*], Guilherme Rosa Franzini[a], Stefano Lenci[b]

[a]*Offshore Mechanics Laboratory - LMO, Escola Politécnica, University of São Paulo, Brazil*
[b]*Università Politecnica delle Marche, Ancona, Italy*

**Abstract**

This paper focuses on the analysis of the parametric excitation of a vertical and immersed flexible rod, showing the influence of the choice of the shape function used in the Galerkin's method. For this, three different reduced-order models (ROMs) are obtained from the continuous equation of transverse motion employing different shape functions. The first model (ROM(i)) uses an approximation of the actual vibration mode of the rod, written as a "Bessel-like" function. The second model (ROM(ii)) is based on a single trigonometric function as the shape function. Finally, a multi-modal ROM (ROM(iii)) is obtained using three trigonometric functions as a set of shape functions. Simulations are carried out aiming at verifying the capability of each model to properly represent the dynamics of the rod under parametric excitation. The quality of the numerical results obtained from the integration of the aforementioned ROMs is assessed by means of a comparison with a solution based on the finite element method. In addition to the numerical analysis, an analytical solution for the steady-state amplitude of a generic Duffing-Mathieu-Morrison oscillator is obtained using the method of multiple scales. A case study is developed using the data of a vertical riser as an example of an engineering application. Maps of the steady-state amplitude as a function of the excitation amplitude and frequency are plotted using both the numerical simulations and the multiple scales solution. The results show that ROM(i) and ROM(iii) are in good agreement with the finite element solution. ROM(i) has the advantage of having only one degree of freedom; the obtained analytical solution can thus be applied to this model. The use of a ROM with one degree of freedom using "Bessel-like" functions in the Galerkin's

---

*Corresponding author
    Email address:* `guilherme.jorge.lopes@usp.com.br` (Guilherme Jorge Vernizzi)

scheme is concluded to have clear advantages from the practical point of view. The analytical solution allows this kind of ROM to give a post-critical amplitude map with low computational effort and that is in good agreement with the maps obtained with the simulation of the ROMs.

## 1. Introduction

From the point of view of the mathematical model of a dynamical system, the parametric excitation phenomenon occurs when at least one of the parameters of the equations of motion varies explicitly with respect to time. This variation comes
5  from different physical behaviours accordingly to the studied system. The simplest example is the Hill's equation, the differential equation of motion of a linear dynamical system of one degree of freedom (1-DOF) with a time-varying stiffness. When the stiffness variation follows a trigonometric function in time, Hill's equation becomes the classical Mathieu's equation, which has been extensively investigated (see for
10  example [1], [2], [3] and [4]).

As a matter of motivation, the current work is based on the analysis of a vertical flexible rod subjected to top motion excitation. A technological application of the study lies on the offshore engineering scenario, in which a vertical riser is subjected to vertical motions imposed at the top by the first-order response of the floating unit
15  to the wave excitation.

The response of a vertical riser to parametric excitation has been addressed in several works during the last decades. A pioneer work to understand the basic dynamical properties of the problem is [5], in which a hanging string in still fluid is subjected to parametric excitation. This work revealed the essential role of the non-
20  linear hydrodynamic damping to limit the motion amplitude in the unstable regions of Mathieu's equation. In [6], a 1-DOF model for a vertical tether of a TLP (Tension Leg Platform) is investigated and used to construct the Strutt's diagram for the problem. The results showed good agreement with the experimental data at disposal. Another initial study that worth mentioning is the one presented in [7], in which an
25  extensible pendulum under support excitation is investigated. The model with only 2-DOF has a very rich dynamical behaviour, with the parametric resonance condi-

2

tion being similar to the dry 1-DOF model of a TLP. A remarkable result of the latter work is the analytical solution obtained for the problem, which is in very good agreement with conducted experiments presented in the same work.

In [8], the parametric excitation of the vertical tethers of a TLP was investigated. In this study, the variation of tension along the length of the tethers was disregarded, since the data used considered the immersed weight (i.e., the weight minus the buoyance force) to be much smaller than the tension at the upper and lower boundaries. This justified the use of a sinusoidal function as a shape function in the Galerkin's scheme employed aiming at obtaining a 1-DOF model for the problem. The authors used this model to plot a Mathieu stability chart for the linear problem. They also obtained an expression for the steady-state amplitude of the non-linear problem considering a Morrison damping term and applying the averaging method (for the averaging method, see[4]).

The effect of the tension variation due to the immersed weight was kept in the analysis carried out by [9]. The authors investigated the top motion excitations on a vertical extensible cable, applying the Galerkin method using the heavy vertical cable modes of vibration, given by Bessel functions, as shape functions. The results showed that the post-critical amplitude is significantly influenced by the choice of projection function by comparing with the model presented in [8].

The effects of the coupling between modes on the stability of vertical tethers under parametric excitation is investigated in [10]. The axial and transversal dynamics are kept and a Galerkin's projection is applied with some modes of vibration. It is pointed out that the coupled model changes the instability regions in the space of control parameters. In [11], the coupled axial and transversal dynamics is also investigated. In this case, the focus was the internal non-linear resonances in the structure. It is shown that in the undamped coupled model no steady-state solution is obtained. However, when the non-linear Morrison damping is included, the effects of internal resonances are reduced and steady-state solutions are developed. The analysis regarding the non-linear resonances is then expanded in [12]. A multiple scales solution is obtained for the coupled dynamics of the vertical tether under parametric excitation, and the principal parametric resonance is investigated. Another important result is presented in [13], in which the author applies the method of multiple scales both in space and time for the equation of transversal motion. Non-linear

3

modes of vibration are obtained for the structure using the multiple scales solution and the presence of travelling waves during the motion is also detected as a result of the variation of the natural frequency with the position along the length of the beam under varying tension.

All the aforementioned works treat the problem disregarding the axial dynamics, investigating the situation of harmonic and vertical top motion and without the influence of other phenomena. In [14], the parametric excitation of a TLP tether under vertical and horizontal top motions is investigated. In this case, the axial dynamics is kept and the equations of motion are shown not to become Mathieu's equation, but the general Hill's equation. The horizontal top motion also shows to contribute to the parametric excitation. In [15], only the transversal dynamics is considered, but a spectrum of irregular waves is used to describe the top motion. The latter work shows that the responses can be significantly different from those arisen when harmonic excitation is provided to the top. Furthermore, in [16], the multi-frequency parametric excitation is combined with vortex-induced vibrations. One of the major conclusions of that work is that the parametric excitation can significantly amplify the structural response due to vortex-induced vibrations. Finally, in [17], the concomitant effects of vortex-induced vibrations and parametric excitation on a flexible rod are experimentally investigated. It was observed that the imposed motion causes modulation of the response amplitude and also enrich the amplitude spectra.

Since the chosen shape functions can have significant effects on the analysis, it is natural to seek functions that correspond more closely to the vibration modes of the structure. The present work uses the so called "Bessel-like" modes previously presented in [18]. The authors, inspired by a solution made for vertical cables obtained in [19], obtained a closed-form solution for the non-linear modes of vibration of a vertical flexible rod, keeping the effects of bending stiffness and varying tension.The linear modes of vibration incorporating both effects can be obtained as a particular case of the formulation presented. The modes incorporating bending and varying geometrical stiffness could also be obtained using the boundary layer method as it is done in [20]. It is also important to mention that the obtaining of ROMs that can give a better representation of the structure is desirable for other problems in the practice of the offshore engineering. In [21] the stability of two different platforms

under wave action is investigated as study case. In that work the tethers are treated using 1-DOF models. In [22] and [23] a vertical riser under vortex-induced vibrations is investigated using ROMs. In those works, a Galerkin's projection is applied to the equations of motion, and then the model is reduced using the NNM (nonlinear normal modes) approach (For the NNM, see [24]). Those examples show that the obtaining of better ROMs is interesting for different applications.

Lately, some studies have been conducted with reduced-order models (ROMs), in which the effects of the use of different shape functions can be compared. In [25] and [26], the influence of hydrodynamic coefficients on the post-critical amplitude response were investigated using 1-DOF ROMs The difference between both lies mainly on the shape function used, being a sinusoidal function used in the first paper and a "Bessel-like" mode in the second.

In [27] and [28], ROMs are conceived and the results are compared with experimental data. These works show that the ROM based on "Bessel-like" functions are in good agreement with the experimental results, both in the magnitude of the motion displacement and the qualitative behaviour of the dynamics along time. The idea of investigating the problem with simpler projections functions but more DOFs is presented in [29]. In that work, a vertical beam under parametric excitation without considering the Morrison damping is modelled using a 3-DOF ROM based on trigonometric functions. The results are compared to finite element simulations and show good agreement for the amplitude response near the middle point of the beam. In [30], a detailed analysis for the vertical beam, including the Morrison damping, is made with a ROM obtained using three sinusoidal functions. Comparisons are also made with a ROM obtained with a single sinusoidal function. However, the analysis are focused on the response of each degree of freedom alone, with no deep investigation on the composed motion. In the conclusion drawn in [30], the authors indicate as future work the comparison of the ROM derived there with a ROM obtained with a "Bessel-like" functions. This suggestion is followed in the present work.

The aforementioned works on ROMs for the problem parametric excitation of flexible rods focused on the behaviour around the principal parametric resonance of the first vibration mode. Additionally, some of the papers presented post-critical amplitude maps obtained as a result of a huge amount of numerical simulations.

5

The objective of this study is thus to compare the performance of different ROMs for parametric excitation of a slender and immersed vertical rod considering the first mode in the benchmark comparison. Besides the study showing the sensitivity of the response with respect to the choice of the projection function to be applied to the Galerkin's method, analytical solutions for the post-critical amplitudes are obtained. The results are compared with finite element solutions for some excitation amplitudes in the principal parametric resonance. It is worth to notice that in the previously mentioned works, no direct comparison between ROMs based on trigonometric shape functions and a ROM based in "Bessel-like" modes is made and is a novelty of the present contribution. Another novel contribution herein presented is the post-critical amplitude map obtained by applying a perturbation method to the 1-DOF ROM. This type of map is obtained with very low computational cost and very well agrees with the results arisen from the extensive numerical integrations of the ROM.

The paper is structured as follows. In section 2, the model for the continuous problem is presented. Sections 3 and 4 bring the derivation of the 1-DOF and 3-DOFs ROMs respectively. Section 5 presents the development of an analytical solution for the post-critical amplitudes using the method of multiple scales ([4]) in the 1-DOF ROMs. The results are presented and discussed in section 6. Finally, section 7 brings the conclusions.

## 2. Continuous model

Prior to the development of the ROMs, the formulation of the equations of motion for the continuous domain is needed. Only the more important steps of the derivation are shown. Details can be found, for example, in [31].

We here consider the problem of a vertical and flexible rod, with $\mu$ and $\mu_a$ being the structural mass and the added mass per unit length respectively. The rod has unstretched length $L$ and products of axial and bending stiffness $EA$ and $EI$ respectively. A basic sketch with axis definition can be found in Figure 1. For the static problem, the tension along the rod is given by $T(Z) = T_b + \gamma Z$, $T_b$ being the tension at the bottom, $\gamma$ is the submerged weight of the riser, and $Z$ is the axial coordinate, considered zero at the bottom section. Care need to be taken with the tension values, since for very long rods the value of $T_b$ can be negative if the initial applied top
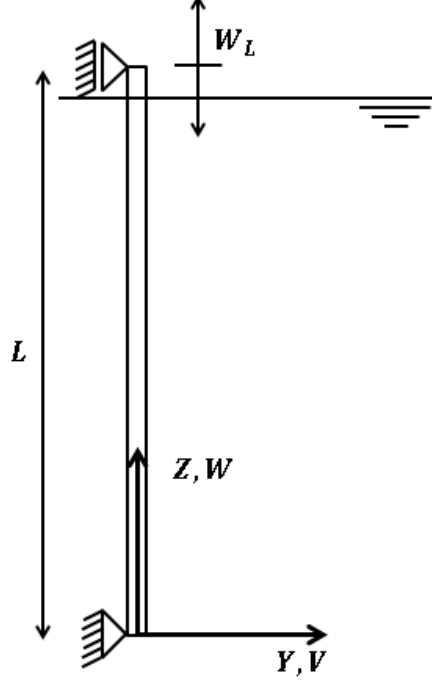
6

tension is not large enough.



Figure 1: Basic sketch for the problem in study. A vertical and flexible rod immersed in fluid under vertical top motion excitation.

Defining $W$ and $V$ as the displacements in the axial and transversal directions respectively, $Y$ the coordinate of a point in relation to the cross-section axis, and assuming a Bernoulli-Euler beam model, the strain at a point $P$ on the cross section can be written as ([31]):

$$\varepsilon_P = W_P' + \frac{1}{2}\left(W_P'\right)^2 + \frac{1}{2}\left(V_P'\right)^2 \cong W' - YV'' + \frac{1}{2}\left(V_P'\right)^2 \tag{1}$$

Along the paper, primes are used to denote differentiation with respect to $Z$. The extended Hamilton's principle is used to take into account the structural damping and Morrison drag force. The principle then reads:

$$\int_{t_1}^{t_2}\left(\delta\mathscr{T} - \delta\mathscr{V} - \left(c\dot{V} + \frac{1}{2}\rho D\overline{C_D}\left|\dot{V}\right|\dot{V}\right)\delta V\right)\mathrm{d}t = 0 \tag{2}$$

Dots are used to represent differentiation with respect to time, as usual. The structural damping constant per unit length is $c$, $\rho$ is the surrounding fluid specific mass, $D$ is the external diameter of the rod, and $\overline{C_D}$ is the mean drag coefficient.

7

Considering the results presented in [31], the differential equations of motion for the problem are then:

$$\mu \ddot{W} + \gamma - EA \left( W'' + V'V'' \right) = 0 \tag{3}$$

$$\left( \mu + \mu_a \right) \ddot{V} + c\dot{V} + \frac{1}{2} \rho D \overline{C_D} \left| \dot{V} \right| \dot{V}$$
$$- EA \left( W''V' + W'V'' + \frac{3}{2} \left( V' \right)^2 V'' \right) + EIV^{\mathrm{IV}} = 0 \tag{4}$$

Following [31], the inertial effects in the axial direction are neglected, allowing for a static condensation procedure. Applying this and integrating equation (3), one obtains:

$$-\frac{\gamma Z}{EA} + W' + \frac{1}{2} \left( V' \right)^2 = \varepsilon_0 \tag{5}$$

The axial strain $\varepsilon_0$ is then obtained using an averaging procedure. The integration of equation (5) along the length of the riser leads to:

$$\varepsilon_0 = \frac{W_L}{L} + \frac{1}{2L} \int_0^L \left( V' \right)^2 \, \mathrm{d}Z - \frac{\gamma L}{2EA} \tag{6}$$

The term $W_L$ stands for the applied displacement at the top. Using equations (5) and (6), the dependence on $W$ in equation (4) can be eliminated, leading to:

$$\left( \mu + \mu_a \right) \ddot{V} + c\dot{V} + \frac{1}{2} \rho D \overline{C_D} \left| \dot{V} \right| \dot{V} + EIV^{\mathrm{IV}} - \gamma V' - \gamma Z V'' - T_b V''$$
$$- \frac{EA}{L} W_{L,d} V'' - \frac{EA}{2L} V'' \int_0^L \left( V' \right)^2 \, \mathrm{d}Z = 0 \tag{7}$$

The top motion was separated into statical and dynamical components. The static component being the displacement of the rod under a tension given by $T_0 = T_b + \gamma Z$. The term $W_{L,d}$ is the dynamical component of the displacement at the top. Note that, disregarding the terms related to structural damping, top motion, and drag force, equation (7) is the same as the one used in [18] to obtain non-linear modes of vibration for a vertical flexible rod.

### 3. 1-DOF reduced-order models

The derivation of both 1-DOF ROMs is grouped, since the procedure to obtain the models is the same and leads to equations of motion that have the same format. The models are obtained using a Galerkin's scheme assuming that the response of the structure can be written as:

$$V(Z,t) = v(t)\psi(Z) \tag{8}$$

For ROM(i), the shape function $\psi$ is a "Bessel-like" mode, herein named as $\psi_b$, obtained in [18]. The expression for $\psi_b$ for the $m$-th mode is given by equation (9) and the modal shape is shown in figure 2, using the numerical data presented in section 6 for $m = 1$.

$$\psi_b = \sqrt[4]{\frac{T_b + EI(m\pi/L)^2}{T_b + EI(m\pi/L)^2 + \gamma Z}}\sin\left(m\pi\frac{\sqrt{T_b + EI(m\pi/L)^2 + \gamma Z} - \sqrt{T_b + EI(m\pi/L)^2}}{\sqrt{T_b + EI(m\pi/L)^2 + \gamma L} - \sqrt{T_b + EI(m\pi/L)^2}}\right) \tag{9}$$
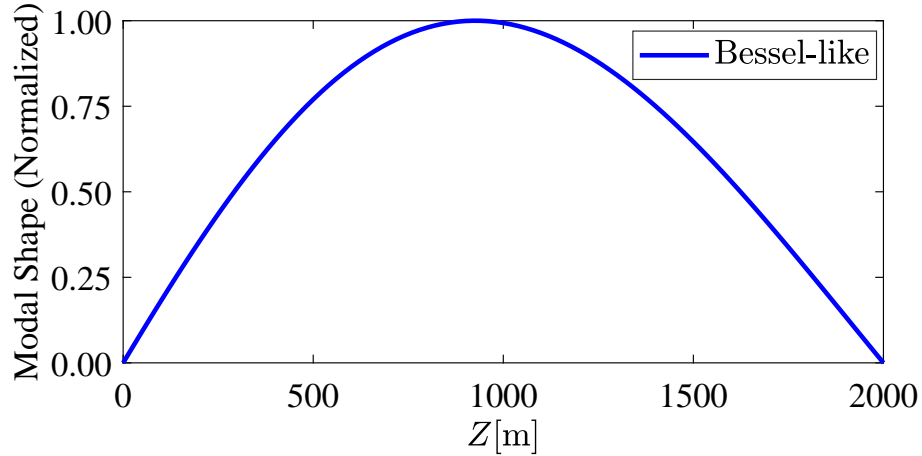


Figure 2: Normalized "Bessel-like" mode. First mode ($m = 1$).

Due to the mathematical expression of this kind of function, analytical expressions for the integrals that appear in the Galerkin's scheme are not available, the reason why those integrals will be kept as part of the evaluation of the constants of

the ROM. Applying equation (8) on equation (7) and using the Galerkin's projection, the resulting model can be written as:

$$\alpha_1 \ddot{v} + \alpha_2 \dot{v} + \alpha_3 v + \alpha_4 W_{L,d} v + \alpha_5 v^3 + \alpha_6 \dot{v} |\dot{v}| = 0 \tag{10}$$

The definition of the parameters $\alpha_i$ are given in Table 4, Appendix A. From equation (10), the natural frequency for the free linear vibrations of this ROM is given by $\omega_b = \sqrt{\alpha_3/\alpha_1}$. Defining the dimensionless displacement and time as $r = v/D$ and $\tau = \omega_b t$ respectively and considering the top motion as a monochromatic oscillation $W_{L,d} = D\delta \cos(n\tau)$, $n$ being the ratio between the parametric frequency and $\omega_b$, the equation of motion for the ROM becomes:

$$\frac{\mathrm{d}^2 r}{\mathrm{d}\tau^2} + \beta_1 \frac{\mathrm{d}r}{\mathrm{d}\tau} + \left(1 + \beta_2 \delta \cos(n\tau)\right) r + \beta_3 r^3 + \beta_4 \left|\frac{\mathrm{d}r}{\mathrm{d}\tau}\right| \frac{\mathrm{d}r}{\mathrm{d}\tau} = 0 \tag{11}$$

where the parameters $\beta_i$ are also given in Table 4. Equations (10) and (11) keep the same form if a trigonometric shape function $\psi_s$ given by equation (12) is used in the Galerkin's scheme.

$$\psi_s = \sin\left(\frac{m\pi Z}{L}\right) \tag{12}$$

For the sake of clearness, the notation will be changed for the ROM based on one trigonometric shape function, named ROM(ii) from now on, and equations (10) and (11) are written for this case as:

$$a_1 \ddot{v} + a_2 \dot{v} + a_3 v + a_4 W_{L,d} v + a_5 v^3 + a_6 \dot{v} |\dot{v}| = 0 \tag{13}$$

$$\frac{\mathrm{d}^2 r}{\mathrm{d}\tau^2} + b_1 \frac{\mathrm{d}r}{\mathrm{d}\tau} + (1 + b_2 \delta \cos(n\tau)) r + b_3 r^3 + b_4 \left|\frac{\mathrm{d}r}{\mathrm{d}\tau}\right| \frac{\mathrm{d}r}{\mathrm{d}\tau} = 0 \tag{14}$$

For ROM(ii), the natural frequency is defined as $\omega_s = \sqrt{a_3/a_1}$. Still considering ROM (ii), the dimensionless time is given by $\tau = \omega_s t$.

## 4. 3-DOF reduced-order model

For the derivation of the 3-DOF ROM, herein ROM(iii), three sinusoidal functions are used as shape functions, assuming the response of the structure in the

10

form:

$$V(Z,t) = v_1(t)\psi_1(Z) + v_2(t)\psi_2(Z) + v_3(t)\psi_3(Z) \tag{15}$$

The three sine functions are defined as:

$$\psi_1 = \sin\left(\frac{i\pi Z}{L}\right) \tag{16}$$

$$\psi_2 = \sin\left(\frac{j\pi Z}{L}\right) \tag{17}$$

$$\psi_3 = \sin\left(\frac{k\pi Z}{L}\right) \tag{18}$$

The constants $i$, $j$ and $k$ are integer numbers to be chosen according to the desired representation. This type of ROM is proposed here inspired by the analysis and results in [30] considering only the first three modes (i.e., i=1, j=2 and k=3). Applying the Galerkin's scheme, the equations of motion read:

$$a_{11}\ddot{v}_1 + a_{12}\dot{v}_1 + a_{13}v_1 + a_{14}W_{L,d}v_1 + a_{15}v_2 + a_{16}v_3$$
$$+ a_{17}v_1^3 + a_{18}v_1v_2^2 + a_{19}v_1v_3^2 + MR_1 = 0 \tag{19}$$

$$a_{21}\ddot{v}_2 + a_{22}\dot{v}_2 + a_{23}v_2 + a_{24}W_{L,d}v_2 + a_{25}v_1 + a_{26}v_3$$
$$+ a_{27}v_2^3 + a_{28}v_2v_1^2 + a_{29}v_2v_3^2 + MR_2 = 0 \tag{20}$$

$$a_{31}\ddot{v}_3 + a_{32}\dot{v}_3 + a_{33}v_3 + a_{34}W_{L,d}v_3 + a_{35}v_1 + a_{36}v_2$$
$$+ a_{37}v_3^3 + a_{38}v_3v_1^2 + a_{39}v_3v_2^2 + MR_3 = 0 \tag{21}$$

Terms $MR_i$ stand for the components of the equations that arise from the Morrison drag force term after the Galerkin's projection. Following what has been done for the 1-DOF ROMs, the dimensionless displacements are defined as $r_i = v_i/D$, and the dimensionless time is defined according to the frequency of the mode to be studied $\omega_t$. Using the dimensionless variables and the top motion as $W_{L,d} = D\delta\cos(n\tau)$, the equations of motion become:

$$\ddot{r}_1 + b_{11}\dot{r}_1 + (b_{12} + b_{13}\delta\cos(n\pi))\,r_1 + b_{14}r_2 + b_{15}r_3$$
$$+ b_{16}r_1^3 + b_{17}r_1r_2^2 + b_{18}r_1r_3^2 + \overline{MR}_1 = 0 \qquad (22)$$

$$\ddot{r}_2 + b_{21}\dot{r}_2 + (b_{22} + b_{23}\delta\cos(n\pi))\,r_2 + b_{24}r_1 + b_{25}r_3$$
$$+ b_{26}r_2^3 + b_{27}r_2r_1^2 + b_{28}r_2r_3^2 + \overline{MR}_2 = 0 \qquad (23)$$

$$\ddot{r}_3 + b_{31}\dot{r}_3 + (b_{32} + b_{33}\delta\cos(n\pi))\,r_3 + b_{34}r_1 + b_{35}r_2$$
$$+ b_{36}r_3^3 + b_{37}r_3r_1^2 + b_{38}r_3r_2^2 + \overline{MR}_3 = 0 \qquad (24)$$

The parameters of equations (22) to (24) are shown in Table 5, Appendix A. Note that, for this kind of model, the integral of the Galerkin's projection over the Morrison drag force term must be evaluated at each time-step due to the absolute value function. On the other hand, for the 1-DOF ROMs, only the motion variable would appear inside the absolute value function. Terms $\overline{MR}_x$ can be put in the general form:

$$\overline{MR}_x = \frac{\rho D^2\overline{C_D}}{2a_{x1}}\int_0^L \psi_x\,\left|\dot{r}_i\psi_i + \dot{r}_j\psi_j + \dot{r}_k\psi_k\right|\left(\dot{r}_i\psi_i + \dot{r}_j\psi_j + \dot{r}_k\psi_k\right)\,\mathrm{d}Z \qquad (25)$$

Another interesting feature of the 3-DOF ROM is the approximation used for computing the natural frequency. Two possibilities can arise, depending on the interpretation given to the approximation used for the natural frequency. In this work, the linearized natural frequencies estimated by the 3-DOF ROM are adopted as the natural frequencies of the dynamical system given by equations (19) to (21). However, one could see the approximated natural frequencies as an inherent characteristic of the shape functions. In this case, the estimative of the natural frequency related to one shape function would be defined as the natural frequency of the oscillator obtained by making a Galerkin's projection with only the corresponding shape function as component of the structural response. The latter approximation is the one used in [30].

12

### 5. Multiple Scales solution

For the 1-DOF ROMs (ROM (i) and ROM (ii)), in which the spatial integral of Galerkin's projection of the Morrison term can be solved analytically, solutions using the method of multiple scales ([32]) can be found. It is important to mention that the multiple scale solution herein proposed can be applied to any oscillator whose equation of motion can be put in the form of a Duffing-Mathieu-Morrison oscillator as in equation (11). To use the method, a small parameter $\epsilon$ is created such that the relations $\beta_1 = \zeta_1 \epsilon$, $\beta_2 \delta = \zeta_2 \epsilon$, $\beta_3 = \zeta_3 \epsilon$ and $\beta_4 = \zeta_4 \epsilon$ hold. Two time scales are used, namely, $\tau_0 = \tau$ and $\tau_1 = \tau \epsilon$. The solution is sough in the form:

$$r = r_0\left(\tau_0, \tau_1\right) + \epsilon r_1\left(\tau_0, \tau_1\right) \tag{26}$$

The equation of motion becomes:

$$\frac{\mathrm{d}^2 r}{\mathrm{d}\tau^2} + \zeta_1 \epsilon \frac{\mathrm{d}r}{\mathrm{d}\tau} + \left(1 + \zeta_2 \epsilon \cos\left(n\tau\right)\right) r + \zeta_3 \epsilon r^3 + \zeta_4 \epsilon \left|\frac{\mathrm{d}r}{\mathrm{d}\tau}\right| \frac{\mathrm{d}r}{\mathrm{d}\tau} = 0 \tag{27}$$

The following operators, correct up to order $\epsilon$, are used in the expansions:

$$\frac{\mathrm{d}}{\mathrm{d}\tau} = \frac{\partial}{\partial \tau_0} + \epsilon \frac{\partial}{\partial \tau_1} \tag{28}$$

$$\frac{\mathrm{d}^2}{\mathrm{d}\tau^2} = \frac{\partial^2}{\partial \tau_0^2} + 2\epsilon \frac{\partial^2}{\partial \tau_0 \partial \tau_1} \tag{29}$$

Now, applying the operators defined by equations (28) and (29) to equation (27) and collecting terms of equal powers in $\epsilon$, the following equations are obtained:

$$\frac{\partial^2 r_0}{\partial \tau_0^2} + r_0 = 0 \tag{30}$$

$$\frac{\partial^2 r_1}{\partial \tau_0^2} + r_1 = -2\frac{\partial^2 r_0}{\partial \tau_0 \partial \tau_1} - \zeta_1 \frac{\partial r_0}{\partial \tau_0} - \zeta_2 \cos\left(n\tau\right) r_0$$
$$-\zeta_3 r_0^3 - \zeta_4 \left|\frac{\partial r_0}{\partial \tau_0}\right| \frac{\partial r_0}{\partial \tau_0} \tag{31}$$

The solution for equation (30) is well-known, and can be written as:

$$r_0 = B_1\left(\tau_1\right) e^{i\tau_0} + c.c. \tag{32}$$

13

For the multiple scale analysis, $i$ is the imaginary constant and "$c.c.$" means the complex conjugate of the terms before it. Now, before substituting equation (32) into equation (31) some strategies are adopted to deal with the quadratic term and the parametric excitation. Following [4], the quadratic damping term is expanded in Fourier series, allowing to write it in terms of the harmonic components and verify which are relevant for eliminating the secular terms present in equation (31). The parametric excitation is treated using the strategy employed in [4] for harmonic forcing. In order to analyse the effects of the parametric excitation around the principal instability region in the Mathieu chart, the parameter $n$ is defined as:

$$n = 2 + \epsilon\sigma \tag{33}$$

with $\sigma$ being the detuning parameter. Applying those assumptions, equation (31) becomes:

$$\frac{\partial^2 r_1}{\partial \tau_0^2} + r_1 = e^{i\tau_0}\left(-2i\frac{\mathrm{d}B_1}{\mathrm{d}\tau_1} - i\zeta_1 B_1 - 3\zeta_3 B_1^2 B_1^* - \frac{\zeta_2 B_1^*}{2}e^{i\sigma\tau_1}\right)$$
$$-e^{i\tau_0}f_1\left(r_0, \frac{\mathrm{d}r_0}{\mathrm{d}\tau_0}\right) + c.c. + N.S.T. \tag{34}$$

Function $f_1$ stands for the term of the Fourier expansion of the quadratic damping that has unitary dimensionless frequency and $N.S.T.$ stands for the non-secular terms of equation (34). Writing the complex function $B_1$ in the polar form $B_1 = R_1 e^{i\theta_1}$, with $R_1 > 0$ and $\theta_1$ being real functions, the solvability condition leads to the complex equation:

$$-2i\frac{\mathrm{d}R_1}{\mathrm{d}\tau_1} + 2R_1\frac{\mathrm{d}\theta_1}{\mathrm{d}\tau_1} - i\zeta_1 R_1 - 3\zeta_3 R_1^3 - \frac{\zeta_2 R_1}{2}e^{-2i\theta_1 + i\sigma\tau_1}$$
$$-\frac{f_1\left(r_0, \frac{\mathrm{d}r_0}{\mathrm{d}\tau_0}\right)}{e^{i\theta_1}} = 0 \tag{35}$$

Using the polar form of equation (32), it is clear that $r_0 = 2R_1\cos(\tau_0 + \theta_1)$. With that, the term arisen from the quadratic damping can be written as:

$$\frac{f_1}{e^{i\theta_1}} =$$

$$\frac{\zeta_4}{2\pi} \int_0^{2\pi} (-2R_1 \sin{(\tau_0 + \theta_1)}) |-2R_1 \sin{(\tau_0 + \theta_1)}| e^{-i(\tau_0 + \theta_1)} d\tau_0 =$$

$$\frac{16 i R_1^2 \zeta_4}{3\pi} \qquad (36)$$

Separating real and imaginary parts of equation (35), the following system of equations is written:

$$2R_1 \frac{d\theta_1}{d\tau_1} - 3\zeta_3 R_1^3 - \frac{\zeta_2 R_1}{2} \cos{(-2\theta_1 + \sigma\tau_1)} = 0 \qquad (37)$$

$$-2\frac{dR_1}{d\tau_1} - \zeta_1 R_1 - \frac{16 R_1^2 \zeta_4}{3\pi} - \frac{\zeta_2 R_1}{2} \sin{(-2\theta_1 + \sigma\tau_1)} = 0 \qquad (38)$$

Giving continuity to the derivation, the relations given by equation (39) are proposed.

$$\phi = \sigma\tau_1 - 2\theta_1 \Rightarrow 2\frac{d\theta_1}{d\tau_1} = \sigma - \frac{d\phi}{d\tau_1} \qquad (39)$$

After substituting equation 39 in equations (37) and (38), one obtains:

$$R_1 \sigma - R_1 \frac{d\phi}{d\tau_1} - 3\zeta_3 R_1^3 - \frac{\zeta_2 R_1}{2} \cos{(\phi)} = 0 \qquad (40)$$

$$-2\frac{dR_1}{d\tau_1} - \zeta_1 R_1 - \frac{16 R_1^2 \zeta_4}{3\pi} - \frac{\zeta_2 R_1}{2} \sin{(\phi)} = 0 \qquad (41)$$

Since the objective is to search for non-trivial steady state solutions, the derivatives that appear in equations (40) and (41) are taken as zero. Isolating the trigonometric terms of both equations, squaring them and summing up both results lead to:

$$\left(2\sigma - 6\zeta_3 R_1^2\right)^2 + \left(2\zeta_1 + \frac{32}{3\pi} R_1 \zeta_4\right)^2 = \zeta_2^2 \qquad (42)$$

It is clear that equation (42) is a bi-quadratic polynomial expression in the cases in which the linear or the quadratic damping are zero. In the present work, the case of no structural damping is presented ($\zeta_1 = 0$) and the following expression is valid

for the steady state solution:

$$R_1^2 = \frac{\frac{-1024\zeta_4^2}{9\pi^2} + 24\zeta_3\sigma \pm \sqrt{\left(\frac{1024\zeta_4^2}{9\pi^2} - 24\zeta_3\sigma\right)^2 - 144\zeta_3^2\left(4\sigma^2 - \zeta_2^2\right)}}{72\zeta_3^2} \quad (43)$$

When this solution gives a possibility of a real positive value for $R_1$ it can be ap-
plied; otherwise, there is no steady-state solution besides the trivial solution ($R_1 =$
0). Additionally, in the case of non-zero structural damping ($\zeta_1 > 0$), equation (42)
results in a polynomial expression that is not bi-quadratic. This leads to the possi-
bility of more than one positive value of $R_1$ to be a solution of equation (42). This
case is not treated in this work. However, since for this kind of structure the struc-
tural damping is much smaller than the hydrodynamical one, the use of $\zeta_1 = 0$ is a
good approximation for practical situations.

## 6. Results and discussion

Numerical investigations are carried out using the presented ROMs and the fi-
nite element simulations. Also, the numerical results of the 1-DOF ROMs are com-
pared to the multiple scales solution presented. The structural data is presented in
Table 1 and are extraced from [33] and used by [19] as a case study for the applica-
tion of the segmentation method. In [18] this data is used in the numerical example
of the non-linear modes of a vertical rod.

Table 1: Data for the structural model extracted from [33].

| Property | Value |
|----------|-------|
| $(\mu + \mu_a)$ | 1200 kg/m |
| $EI$ | $318.6 \times 10^6$ Nm$^2$ |
| $\gamma$ | 3433.5 N/m |
| $EA$ | $8541.8 \times 10^6$ N |
| $L$ | 2000 m |
| $\rho$ | 1025 kg/m$^3$ |
| $D$ | 0.5588 m |

$\mu_a$ is the potential added mass for a cylinder. The mean drag coefficient is taken
as $\overline{C_D} = 1.0$, and the bottom tension is taken as $T_b = 13.133 \times 10^6$ N. As mentioned

16

before, the results here are focused on the case of null structural damping, that is, $c = 0$ Ns/m$^2$. The parameters of the ROMs with these physical properties can be found in table 6, Appendix A. The different ROMs are numerically integrated using a Runge-Kutta scheme implemented in the ode45 function available in Matlab$^®$. The dimensionless time-step $\Delta\tau = 0.1$ and the total simulation dimensionless time is $\tau_t = 6000$. Post-critical amplitude maps are constructed by taking the average of the peaks in the last 1% of the time-series in order to obtain the steady state amplitude $A_m$. In addition, for the 1-DOF ROMs (ROM(i) and ROM(ii)), the post-critical maps were plotted using the multiple scales solution as well.

Simulations using the finite element method (FEM) are also carried out for the sake of comparison. These higher-order hierarchical models are simulated using the in-house software Giraffe, which has proved to be a useful tool for riser analysis. The rod is modelled using 100 elements composed of three nodes each. The submerged weight, added mass and Morrison drag forces are applied along the elements, while a sinusoidal displacement is applied to the top of the rod. The time integration in Giraffe is made with the Newmark scheme with a self-adjusting time-step along the simulation. Further details regarding Giraffe can be found in [35] and [36]. Not that Giraffe makes use of the finite element described in [34], which is the same element used for modelling the example herein worked.

One of the issues of the amplitude comparison is the fact that each ROM uses a different projection basis. Also, the FEM solution gives the time-series of the displacement of each modelled node. In this study, the displacement field of the rod was constructed for each ROM, using its respective projection functions. Then, the point used for comparison of steady-state amplitude was the one who presented the highest amplitude in each case, being that also adopted for the solution based on the FEM. Note that the point with the highest amplitude is more or less the same between the different cases, as it can be seen in the modal shapes presented in Figure 3. Finally, considering the synchronous vibrations that are obtained in this kind of problem, the value obtained for the maximum displacement amplitude along the span is the most relevant from an engineering point of view.

In order to keep the offshore engineering practice in the view, first-order motions of the floating unit (observed, typically, with periods between 2 and 20 seconds - the same of the sea-waves) are used as a source for the parametric excitation. The natu-

17

ral frequencies of the first mode of the structure obtained from the FEM model and
from the three ROMs are presented in Table 2. As it can be calculated, the first mode
will be under the principal Mathieu instability for waves with a period of 17 seconds. In Table 2 the three frequencies obtained for ROM(iii) and the FEM solution
are presented in ascending order.

Table 2: Natural frequencies calculated by each model.

| Model | Mode | Frequency (rad/s) | Period (s) |
|---|---|---|---|
| FEM | 1 | 0.1833 | 34.3 |
| FEM | 2 | 0.3667 | 17.1 |
| FEM | 3 | 0.5502 | 11.4 |
| ROM(i) | 1 | 0.1836 | 34.2 |
| ROM(ii) | 1 | 0.1643 | 38.2 |
| ROM(iii) | 1 | 0.1839 | 34.2 |
| ROM(iii) | 2 | 0.3674 | 17.1 |
| ROM(iii) | 3 | 0.5552 | 11.3 |

Completing the modal analyses, the shapes of the first mode of vibration are
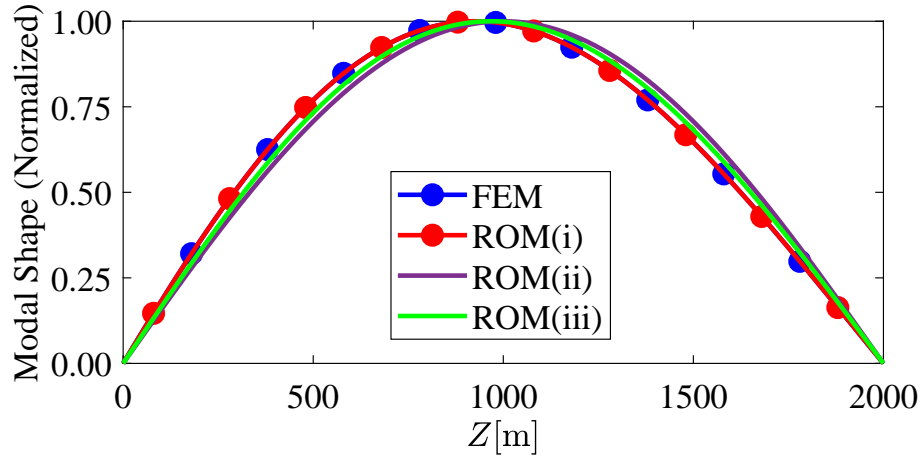compared in Figure 3.



Figure 3: Normalized modes of vibration for each model. Modal shape comparison.

The "Bessel-like" function is clearly the one suitable to represent the modes of

vibration of this type of structure. Also, considering the results shown in Table 2, the use of a single trigonometric function to obtain a ROM for the problem is clearly not adequate in modal terms.

Figures 4 and 5 show the post-critical amplitude maps numerically and analytically obtained from the analysis of ROM(i). In turn, Figures 6 and 7 show the same maps resulting from ROM(ii).



Figure 4: Post critical amplitude map for ROM(i) in color-scale. Numerical integration results. $n$ indicating the dimensionless frequency of the imposed motion, $A_m$ the steady-state amplitude and $\delta$ indicating the dimensionless amplitude of the imposed motion.

Figure 5: Post critical amplitude map for ROM(i) in color-scale based on the multiple scale analysis. $n$ indicating the dimensionless frequency of the imposed motion, $A_m$ the steady-state amplitude and $\delta$ indicating the dimensionless amplitude of the imposed motion.
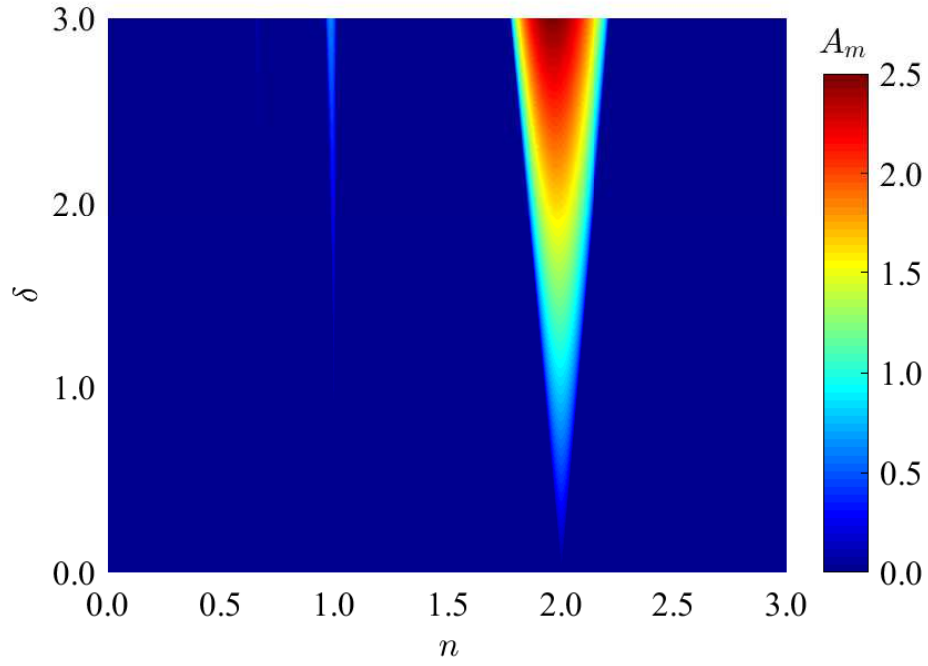
Figure 6: Post critical amplitude map for ROM(ii) in color-scale. Numerical integration results. $n$ indicating the dimensionless frequency of the imposed motion, $A_m$ the steady-state amplitude and $\delta$ indicating the dimensionless amplitude of the imposed motion.
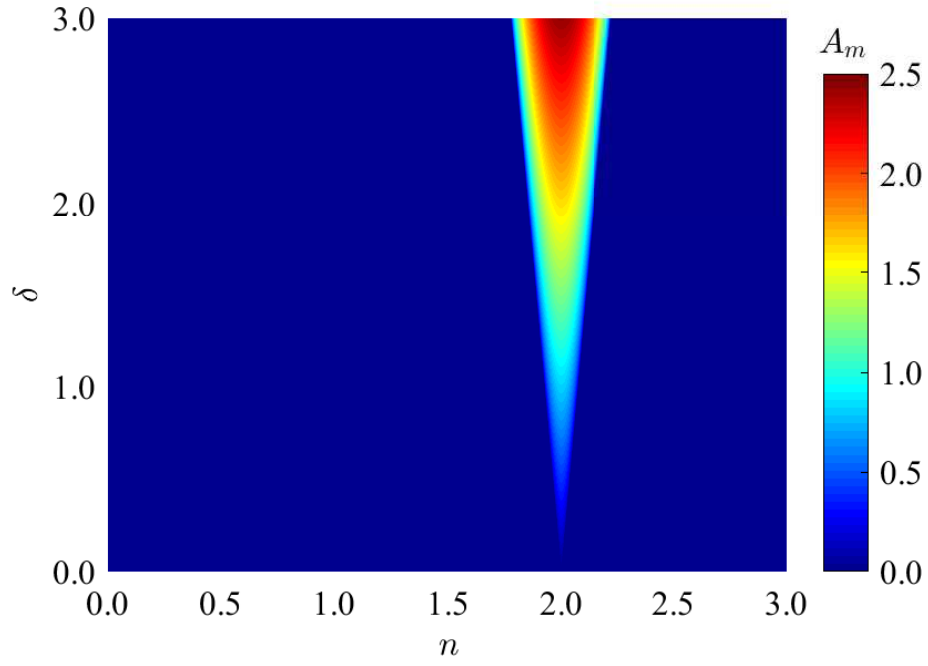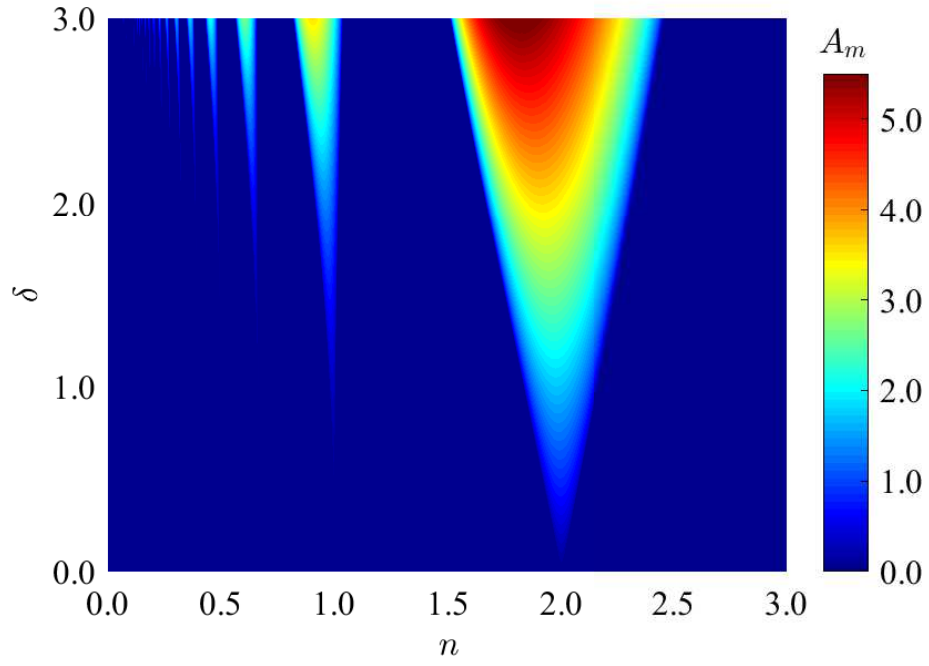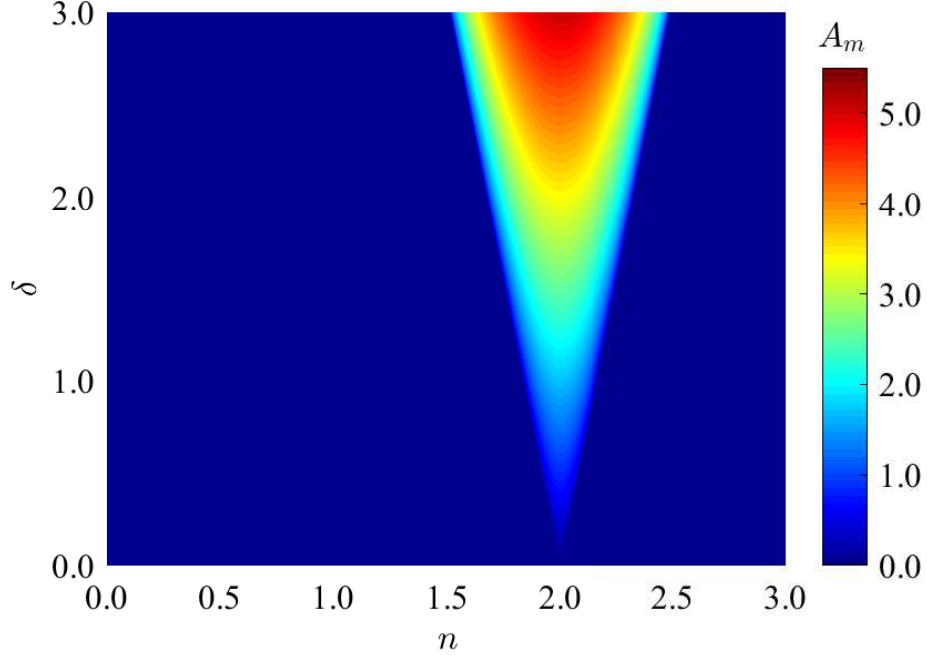
Figure 7: Post critical amplitude map for ROM(ii) in color-scale based on the multiple scale analysis. $n$ indicating the dimensionless frequency of the imposed motion, $A_m$ the steady-state amplitude and $\delta$ indicating the dimensionless amplitude of the imposed motion.

As it can be noticed from the analysis of Figures 4 to 7, there is a good agreement between the multiple scales solution and the values obtained using numerical integration of the equations of motion that govern the ROMs. One noticeable limitation of the analytical solution is the prediction of the frequency with the highest amplitude as the amplitude of the parametric excitation grows. Another limitation is that only the region close to the principal parametric excitation is captured by the analytical solution. Notice, however, that focus is placed in the latter region.

Two major differences are noticed between the results in Figures 4 and 6. First, the amplitudes of steady-state motion are higher for ROM(ii). Second, there are more regions of non-zero motion in Figure 6. The number of those regions and the post-critical amplitude of response within them grow quickly with the amplitude of the parametric excitation. This occurs because, since the stiffness obtained in ROM(ii) is smaller, those regions start at lower values of $\delta$. Since the frequency range is the same, the number of regions is larger in figure 6.

22

Now, for ROM(iii), the post-critical amplitude map is shown in Figure 8. The map is plotted using equation (15) for a particular point along the riser. For that purpose, the displaced position of the riser is recovered from the shape functions and the displacement time-series of one point is used to calculate the steady-state amplitude. The point considered is the one with unitary displacement on the modal shape presented in Figure 3, at $Z = 968$ m.
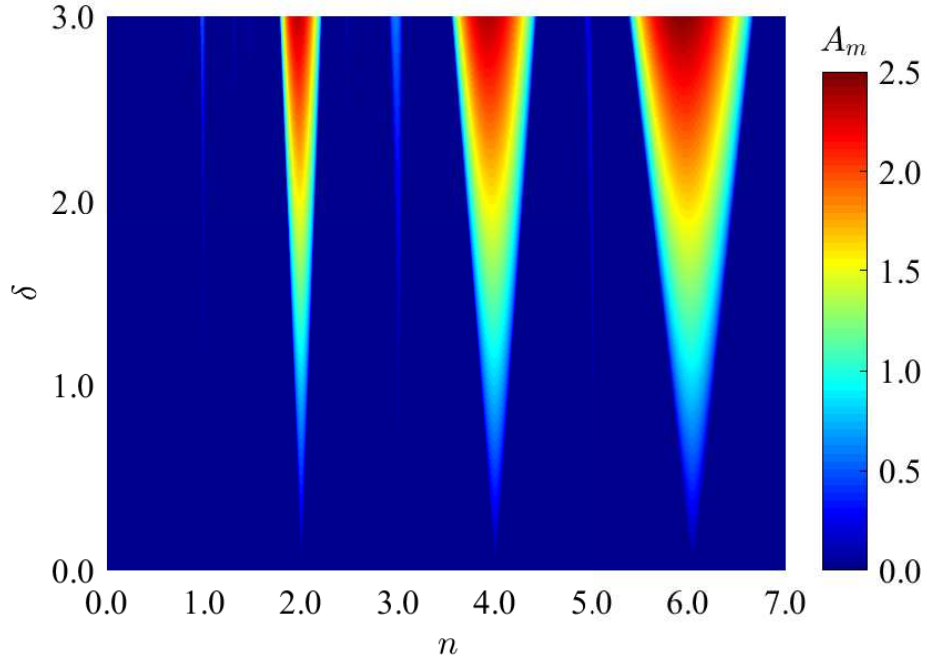


Figure 8: Post critical amplitude map for ROM(iii) in color-scale. Numerical integration results. $n$ indicating the dimensionless frequency of the imposed motion, $A_m$ the steady-state amplitude and $\delta$ indicating the dimensionless amplitude of the imposed motion.

In Figure 8, The areas of steady-state response for three modes can be seen. In the region corresponding to the first mode, it can be seen that ROM(iii) and ROM(i) give results that are in agreement with each other, showing that in terms of representation of the mode in study, both approaches wield similar results. This can be better seen in Figure 9 where focus is placed on the principal parametric resonance of the first mode.

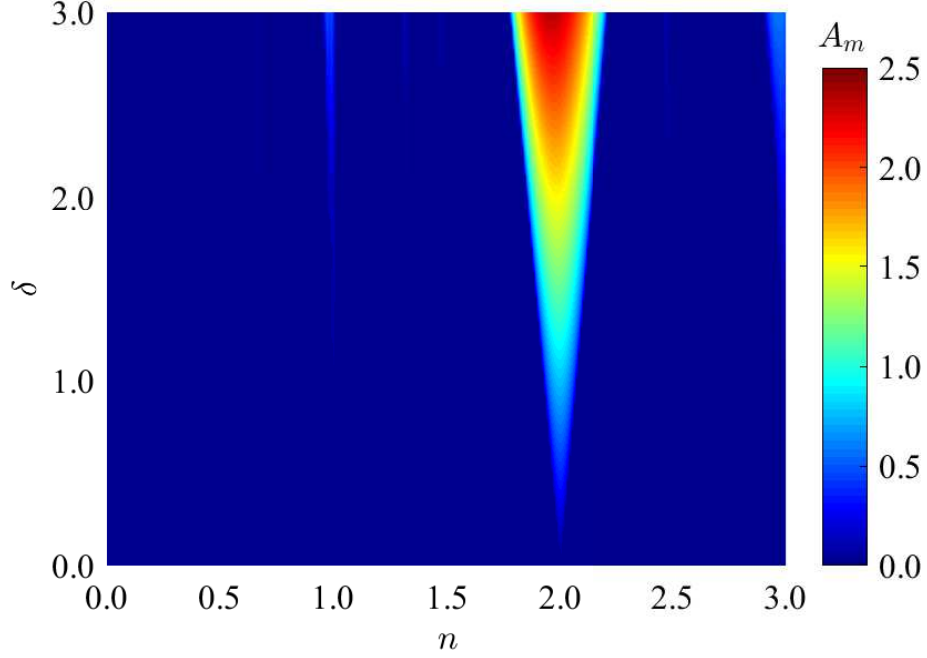Figure 9: Post critical amplitude map for ROM(iii) in color-scale around the principal parametric excitation of the first mode. Numerical integration results. $n$ indicating the dimensionless frequency of the imposed motion, $A_m$ the steady-state amplitude and $\delta$ indicating the dimensionless amplitude of the imposed motion.

In order to state the agreement of each ROM with an adopted reference, comparisons with the FEM solution are made. Figure 10 depicts the evolution curves of the steady-state amplitude with respect to the parametric excitation amplitude over the principal parametric resonance ($n = 2$). For the FEM solution, the point with the highest displacement during the motion is considered, which corresponds to the modal amplitude in the case of ROM(i). Due to the presence of Morrison's quadratic damping, the point where the curves in Figure 10 start ascending in response amplitude is not the origin. Bellow the values of dimensionless excitation amplitude $\delta$ needed to start non-trivial responses, the stable solution is the trivial one. This feature can be seen in Figure 11.

Figure 10: Post critical amplitude comparison for the different models on the principal parametric resonance ($n = 2$) as function of the dimensionless amplitude of excitation $\delta$.
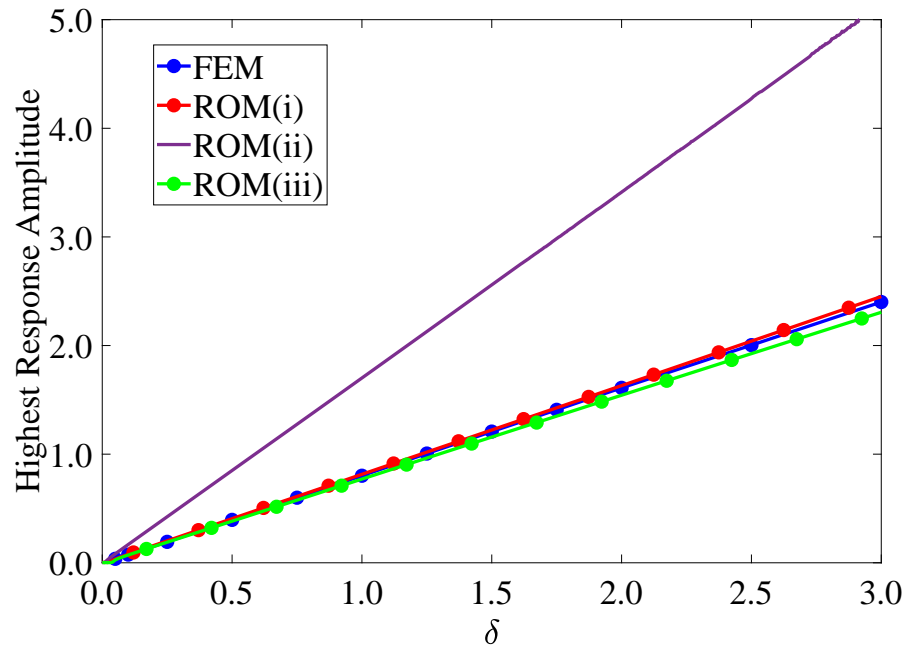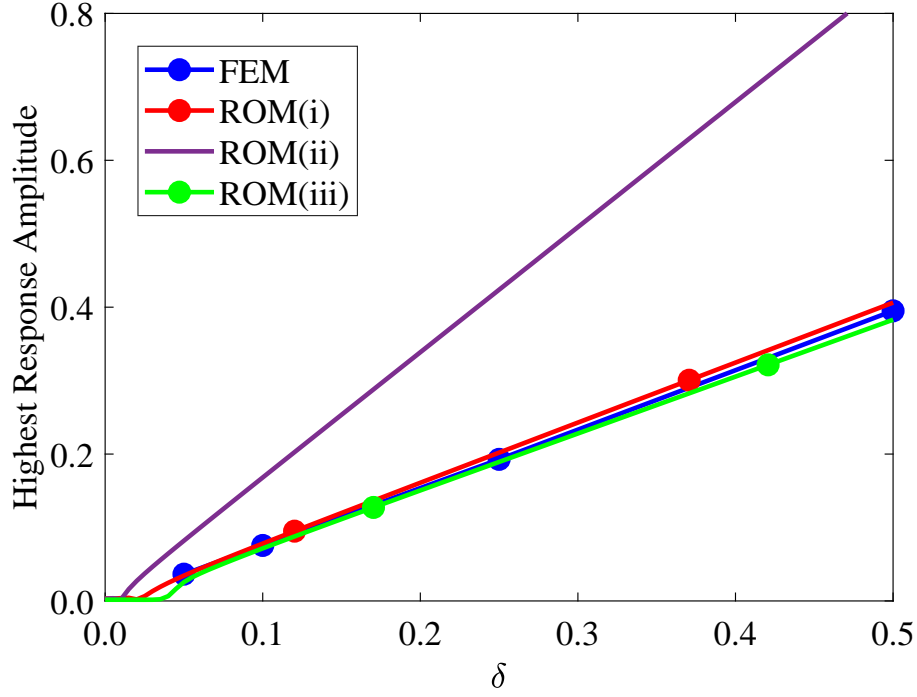
Figure 11: Post critical amplitude comparison for the different models on the principal parametric res-
onance ($n = 2$) as function of the dimensionless amplitude of excitation $\delta$. Focus on the region of small
$\delta$.

As can be noticed, there is a good agreement on the steady-state amplitude pre-
diction between the FEM solution, ROM(i) and ROM(iii). The limit of the results
presented, $\delta = 3$, corresponds to 45% of the model stiffness. Since most of the stiff-
ness is from geometric nature (i.e., that associated with the traction in the rod), this
corresponds to values of axial displacements that are significant for the structural
behaviour. From this point on, the ROMs are expected to start losing accuracy be-
cause they are based on the hypothesis that the axial dynamics can be disregarded.

As can be seen in Figures 4, 6 and 8, there is a widening in the range of excitation
frequencies that causes the models to exhibit a steady-state motion as the ampli-
tude of excitation grows. This means that care should be taken when dealing with
high values of the parametric excitation amplitude. Since the range of frequency
in which there is some response is large in that situation, the interaction between
modes can occur for large excitation amplitudes and the 1-DOF model is not able to
reproduce this phenomenon. However, in engineering applications, the amplitude

of parametric excitations are expected not to be so large. For this case, ROM(i) and ROM(iii) give good results as compared to the finite element solution.

Now, in order to compare the models from a computational point of view, the time required for the simulation of each model is presented in Table 3. All the simulations were carried out in the same standard household desktop without any other tasks running in background. For the ROMs, it was measured the time required to produce the simulations for a 600×600 post-critical amplitude map, resulting in 360000 simulations. The average time of a single simulation was then taken from that global measure. For the FEM the average of ten simulations was taken as the average time for one single simulation and the time required for a 600×600 was estimated with that average.

Table 3: Comparison of computational time required by each type of solution.

| Model | Method | Simulation of a 600x600 map (s) | Single simulation (s) |
|---|---|---|---|
| FEM | Numerical | $483.1 \times 10^6$ | $1.342 \times 10^3$ |
| ROM(i) | Numerical | $29.3 \times 10^3$ | 0.082 |
| ROM(i) | Analytical | $11.5 \times 10^{-3}$ | $3.194 \times 10^{-8}$ |
| ROM(iii) | Numerical | $114.9 \times 10^3$ | 0.319 |

With those results, some advantages of the ROMs and the analytical solution can be drawn. When is desirable to know the response of the structure in some particular frequencies, the ROMs are clearly a faster option in order to give preliminary estimates. Also, the time demanded for a FEM simulation would lead to a high or even impracticable computational time costs in order to do parametric studies, like the one presented by the post-critical amplitude maps. Finally, the analytical solution has a great advantage even in relation to the numerical solution of the ROMs. This turns the analytical solution presented into an useful tool for engineering practice, since it can help defining the study-cases that need a more refined analysis while having a small computational time cost. Note that the analytical solution was only possible for the ROMs with a single DOF and that the quality of this ROM was acquired thanks to the use of the "Bessel-like" function.

Now, to make a qualitative comparison of the responses, the phase space for the four models are presented in Figure 12. For the FEM solution, the displacements and velocities of the point with the highest displacement during the steady-state

27

motion are considered. The simulations presented in the figure represent the case

of the principal parametric resonance, $n = 2$. Two different top motion amplitudes are considered in the comparison, being them $\delta = 0.50$ and $\delta = 3.00$. This is made to give another view of how closely each ROM agrees with the reference case and to show the effects of the motion amplitude in the phase-space portrait.
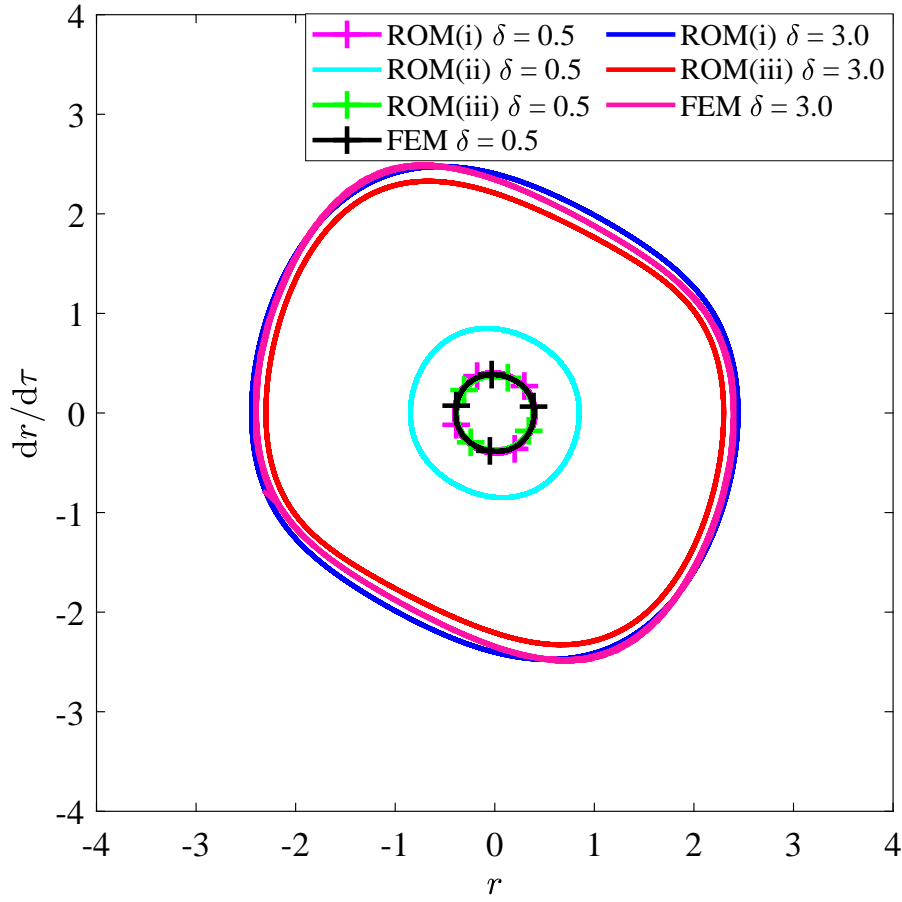


Figure 12: Comparison of the phase space portrait for the steady-state solution with different models and amplitudes. Dimensionless frequency of excitation $n = 2$.

It can be seen from the phase space portraits that both ROM(i) and ROM(iii) are

in good agreement with the numeric reference. Both the amplitude and the shape of the limit cycle are well predicted by those two models. ROM(ii) in its turn presents a larger amplitude for the same excitation. Those results confirm what was previously

28

shown in figure 10. One interesting conclusion can be drawn from the limit cycles with large amplitude, the case with $\delta = 3.00$. ROM(i) reproduces a limit cycle that is more close to the reference in both amplitude and shape than the one produced by ROM(iii), even with the latter having more DOF. This shows that, even with the shape of the "Bessel-like" and the trigonometric functions not being so different, the gains in terms of analysis can be quite different. Also, although the inclusion of more projection functions allowed to obtain good modal shapes and frequencies using trigonometric functions, ROM(i) still remains closer than ROM(iii) to the reference for large amplitudes.

## 7. Final remarks

Three reduced-order models (ROMs) were constructed to analyse the transversal vibrations of an immersed, vertical and flexible rod under parametric excitation. The ROMs were obtained using a Galerkin's scheme with different shape functions. The first ROM (ROM(i)) used one "Bessel-like" function, which is a good approximation to the actual mode of vibration of the structure. For the second ROM (ROM(ii)), one trigonometric function was used as a shape function. Finally, for the third ROM (ROM(iii)), a multi-modal approach was carried out, using three trigonometric functions as shape functions. Finite element simulations (FEMs) were also carried out to be used as a reference to verify the adherence of the ROMs. A riser is considered as a case study and focus is placed on the parametric instability of the first mode.

The models were compared by means of phase space portraits and curves representing the evolution of the steady-state amplitude of response with the variation of the excitation amplitude at the frequency that corresponds to the principal Mathieu's instability. The use of a "Bessel-like" shape function can be concluded to lead to good results if compared to the FEM solution in the range in which the hypothesis of disregarding the axial dynamics is still acceptable. For the models based on trigonometric functions, it is clear that an approach with more than one shape function to approximate the solution is needed, since ROM (ii) has proved to not properly represents the dynamics observed in the FEM solution. Although leading to a more cumbersome algebra in order to obtain the ROM, it is concluded that the use of a "Bessel-like" function is required for a good 1-DOF ROM. This also leads to three gains in analysis terms. First, the problem becomes simpler, as it is reduced to a sin-

29

gle equation of motion. Second, the evaluation of this ROM using numerical tools is faster than for ROM(iii). Finally, an analytical solution for the steady-state amplitude of a generic Duffing-Mathieu-Morrison oscillator was obtained for the case of a single DOF. This requires a good 1-DOF ROM, which is provided by the "Bessel-like" function but not by a trigonometric function.

Additionally, maps of the vibration amplitude as functions of the parametric excitation frequency and amplitude were presented. Those maps were numerically obtained from the ROMs. For the 1-DOF ROMs the maps were also obtained using the analytical solution, showing good agreement with the same maps obtained numerically. The computational time for the construction of those maps were evaluated and compared. ROM(i) is considerably faster than ROM(iii), giving another advantage for the use of a 1-DOF ROM. In addition, the construction of the maps with the analytical solution can be made in a fraction of second, which gives a practical advantage in using a ROM based in the "Bessel-like" function for a vertical rod. This means that preliminary analysis and decisions in the offshore engineering can be made with a very low computational cost for the motivational problem herein investigated. Finally, the use of the ROMs allows for this kind of parametric investigations, that would be very costly in computational time when using the FEM.

Further works include the consideration of the linear structural damping in the analytical solution and investigations regarding the situations where two distinct solutions are predicted. Multi-modal approaches using "Bessel-like" modes instead of the trigonometric functions could be used to determine the value of excitation amplitude over which modal interaction starts to occur. In addition, for values below this one, the post-critical amplitude for the continuous model can be obtained by the superposition of the analytical solution herein presented for various modes of the structure.

**Acknowledgements**

30

# Appendix A

Table 4: Parameters for 1-DOF ROMs.

| Parameter | Expression |
|---|---|
| $\alpha_1$ | $\left(\mu + \mu_a\right)\displaystyle\int_0^L \psi_b\psi_b\,\mathrm{d}Z$ |
| $\alpha_2$ | $c\displaystyle\int_0^L \psi_b\psi_b\,\mathrm{d}Z$ |
| $\alpha_3$ | $\displaystyle\int_0^L EI\psi_b^{\mathrm{IV}}\psi_b - \gamma\psi_b'\psi_b - \gamma Z\psi_b''\psi_b - T_b\psi_b''\psi_b\,\mathrm{d}Z$ |
| $\alpha_4$ | $-\dfrac{EA}{L}\displaystyle\int_0^L \psi_b''\psi_b\,\mathrm{d}Z$ |
| $\alpha_5$ | $-\dfrac{EA}{2L}\displaystyle\int_0^L \psi_b'\psi_b'\,\mathrm{d}Z\displaystyle\int_0^L \psi_b''\psi_b\,\mathrm{d}Z$ |
| $\alpha_6$ | $\dfrac{1}{2}\rho D\overline{C_D}\displaystyle\int_0^L \psi_b^2\left|\psi_b\right|\,\mathrm{d}Z$ |
| $\beta_1$ | $\dfrac{\alpha_2}{\alpha_1\omega_b}$ |
| $\beta_2$ | $\dfrac{D\alpha_4}{\alpha_1\omega_b^2}$ |
| $\beta_3$ | $\dfrac{D^2\alpha_5}{\alpha_1\omega_b^2}$ |
| $\beta_4$ | $\dfrac{D\alpha_6}{\alpha_1}$ |
| $a_1$ | $\left(\mu + \mu_a\right)\dfrac{L}{2}$ |
| $a_2$ | $\dfrac{cL}{2}$ |
| $a_3$ | $EI\dfrac{L}{2}\left(\dfrac{m\pi}{L}\right)^4 + \left(\dfrac{m\pi}{L}\right)^2\left(\dfrac{\gamma L^2}{4} + \dfrac{T_b L}{2}\right)$ |
| $a_4$ | $\dfrac{EA}{2}\left(\dfrac{m\pi}{L}\right)^2$ |
| $a_5$ | $\dfrac{EAL}{8}\left(\dfrac{m\pi}{L}\right)^4$ |
| $a_6$ | $\dfrac{2}{3\pi}\rho DL\overline{C_D}$ |
| $b_1$ | $\dfrac{a_2}{a_1\omega_s}$ |
| $b_2$ | $\dfrac{Da_4}{a_1\omega_s^2}$ |
| $b_3$ | $\dfrac{D^2 a_5}{a_1\omega_s^2}$ |
| $b_4$ | $\dfrac{Da_6}{a_1}$ |

Table 5: Parameters for 3-DOF ROM.

| Term | Expression | Term | Expression |
|---|---|---|---|
| $a_{11}$ | $\left(\mu+\mu_a\right)L/2$ | $a_{12}$ | $cL/2$ |
| $a_{21}$ | $\left(\mu+\mu_a\right)L/2$ | $a_{22}$ | $cL/2$ |
| $a_{31}$ | $\left(\mu+\mu_a\right)L/2$ | $a_{32}$ | $cL/2$ |
| $a_{13}$ | $\dfrac{EIL}{2}\left(\dfrac{i\pi}{L}\right)^4+\left(\dfrac{i\pi}{L}\right)^2\left(\dfrac{\gamma L^2}{4}+\dfrac{T_bL}{2}\right)$ | $a_{14}$ | $\dfrac{EA}{2}\left(\dfrac{i\pi}{L}\right)^2$ |
| $a_{23}$ | $\dfrac{EIL}{2}\left(\dfrac{j\pi}{L}\right)^4+\left(\dfrac{j\pi}{L}\right)^2\left(\dfrac{\gamma L^2}{4}+\dfrac{T_bL}{2}\right)$ | $a_{24}$ | $\dfrac{EA}{2}\left(\dfrac{j\pi}{L}\right)^2$ |
| $a_{33}$ | $\dfrac{EIL}{2}\left(\dfrac{k\pi}{L}\right)^4+\left(\dfrac{k\pi}{L}\right)^2\left(\dfrac{\gamma L^2}{4}+\dfrac{T_bL}{2}\right)$ | $a_{34}$ | $\dfrac{EA}{2}\left(\dfrac{k\pi}{L}\right)^2$ |
| $a_{15}$ | $\gamma\left(i\pi\right)^2\left(\dfrac{2\cos\left(i\pi\right)\cos\left(j\pi\right)-2}{\left(i^2-j^2\right)^2\pi^2}\right)ij$ | $a_{16}$ | $\gamma\left(i\pi\right)^2\left(\dfrac{2\cos\left(i\pi\right)\cos\left(k\pi\right)-2}{\left(i^2-k^2\right)^2\pi^2}\right)ik$ |
| $a_{25}$ | $a_{15}\left(\dfrac{j}{i}\right)^2$ | $a_{26}$ | $\gamma\left(j\pi\right)^2\left(\dfrac{2\cos\left(j\pi\right)\cos\left(k\pi\right)-2}{\left(j^2-k^2\right)^2\pi^2}\right)jk$ |
| $a_{35}$ | $a_{16}\left(\dfrac{k}{i}\right)^2$ | $a_{36}$ | $a_{26}\left(\dfrac{k}{j}\right)$ |
| $a_{17}$ | $\dfrac{EAL}{8}\left(\dfrac{i\pi}{L}\right)^4$ | $a_{18}$ | $\dfrac{EAL}{8}\left(\dfrac{i\pi}{L}\right)^2\left(\dfrac{j\pi}{L}\right)^2$ |
| $a_{27}$ | $\dfrac{EAL}{8}\left(\dfrac{j\pi}{L}\right)^4$ | $a_{28}$ | $\dfrac{EAL}{8}\left(\dfrac{i\pi}{L}\right)^2\left(\dfrac{j\pi}{L}\right)^2$ |
| $a_{37}$ | $\dfrac{EAL}{8}\left(\dfrac{k\pi}{L}\right)^4$ | $a_{38}$ | $\dfrac{EAL}{8}\left(\dfrac{i\pi}{L}\right)^2\left(\dfrac{k\pi}{L}\right)^2$ |
| $a_{19}$ | $\dfrac{EAL}{8}\left(\dfrac{i\pi}{L}\right)^2\left(\dfrac{k\pi}{L}\right)^2$ | $b_{11}$ | $a_{12}/\left(a_{11}\omega_2\right)$ |
| $a_{29}$ | $\dfrac{EAL}{8}\left(\dfrac{j\pi}{L}\right)^2\left(\dfrac{k\pi}{L}\right)^2$ | $b_{21}$ | $a_{22}/\left(a_{21}\omega_2\right)$ |
| $a_{39}$ | $\dfrac{EAL}{8}\left(\dfrac{j\pi}{L}\right)^2\left(\dfrac{k\pi}{L}\right)^2$ | $b_{31}$ | $a_{32}/\left(a_{31}\omega_2\right)$ |
| $b_{12}$ | $a_{13}/\left(a_{11}\omega_2^2\right)$ | $b_{13}$ | $a_{14}D/\left(a_{11}\omega_2^2\right)$ |
| $b_{22}$ | $a_{23}/\left(a_{21}\omega_2^2\right)$ | $b_{23}$ | $a_{24}D/\left(a_{21}\omega_2^2\right)$ |
| $b_{32}$ | $a_{33}/\left(a_{31}\omega_2^2\right)$ | $b_{33}$ | $a_{34}D/\left(a_{31}\omega_2^2\right)$ |
| $b_{14}$ | $a_{15}/\left(a_{11}\omega_2^2\right)$ | $b_{15}$ | $a_{16}/\left(a_{11}\omega_2^2\right)$ |
| $b_{24}$ | $a_{25}/\left(a_{21}\omega_2^2\right)$ | $b_{25}$ | $a_{26}/\left(a_{21}\omega_2^2\right)$ |
| $b_{34}$ | $a_{35}/\left(a_{31}\omega_2^2\right)$ | $b_{35}$ | $a_{36}/\left(a_{31}\omega_2^2\right)$ |
| $b_{16}$ | $a_{17}D^2/\left(a_{11}\omega_2^2\right)$ | $b_{17}$ | $a_{18}D^2/\left(a_{11}\omega_2^2\right)$ |
| $b_{26}$ | $a_{27}D^2/\left(a_{21}\omega_2^2\right)$ | $b_{27}$ | $a_{28}D^2/\left(a_{21}\omega_2^2\right)$ |
| $b_{36}$ | $a_{37}D^2/\left(a_{31}\omega_2^2\right)$ | $b_{37}$ | $a_{38}D^2/\left(a_{31}\omega_2^2\right)$ |
| $b_{18}$ | $a_{19}D^2/\left(a_{11}\omega_2^2\right)$ | | |
| $b_{28}$ | $a_{29}D^2/\left(a_{21}\omega_2^2\right)$ | | |
| $b_{38}$ | $a_{39}D^2/\left(a_{31}\omega_2^2\right)$ | | |

Table 6: Numerical parameters.

| Par. | Value | Par. | Value | Par. | Value | Par. | Value |
|------|-------|------|-------|------|-------|------|-------|
| $\beta_1$ | 0 | $\beta_2$ | 0.1475 | $\beta_3$ | $0.0092 \times 10^{-2}$ | $\beta_4$ | 0.1072 |
| $b_1$ | 0 | $b_2$ | 0.3251 | $b_3$ | $0.0126 \times 10^{-2}$ | $b_4$ | 0.1132 |
| $b_{11}$ | 0 | $b_{12}$ | 1.0075 | $b_{13}$ | 0.1451 | $b_{14}$ | $-0.3009$ |
| $b_{15}$ | 0 | $b_{16}$ | $0.0100 \times 10^{-2}$ | $b_{17}$ | $0.0400 \times 10^{-2}$ | $b_{18}$ | $0.0901 \times 10^{-2}$ |
| $b_{21}$ | 0 | $b_{22}$ | 4.0307 | $b_{23}$ | 0.5806 | $b_{24}$ | $-0.0752$ |
| $b_{25}$ | $-0.7312$ | $b_{26}$ | 0.0016 | $b_{27}$ | $0.0400 \times 10^{-2}$ | $b_{28}$ | 0.0036 |
| $b_{31}$ | 0 | $b_{32}$ | 9.0713 | $b_{33}$ | 1.3063 | $b_{34}$ | 0 |
| $b_{35}$ | $-0.3250$ | $b_{36}$ | 0.0081 | $b_{37}$ | $0.0901 \times 10^{-2}$ | $b_{38}$ | 0.0036 |

# References

[1] L. Meirovitch, Analytical Methods in Vibrations, Macmillan, 1967 (1967).

[2] H. H. E. Leipholz, Stability theory, Academic Press, 1970 (1970).

[3] C. M. Bender, S. A. Orszag, Advanced Mathematical Methods for Scientists and Engineers, McGraw-Hill, 1978 (1978).

[4] A. H. Nayfeh, D. T. Mook, Nonlinear oscillations, John Wiley & Sons, 1979 (1979).

[5] C. Hsu, The response of a parametrically excited hanging string in fluid, Journal of Sound and Vibration 39 (3) (1975) 305–316 (apr 1975). doi:10.1016/s0022-460x(75)80084-8.

[6] R. C. T. Rainey, The dynamics of tethered platforms, Transactions of the Royal Institution of Naval Architects (1977) 59–80 (1977).

[7] C. E. N. Mazzilli, A theoretical and experimental analysis of support-excited non-linear vibrations of the extensible pendulum, IMA Journal of Applied Mathematics 34 (2) (1985) 137–154 (1985). doi:10.1093/imamat/34.2.137.

[8] M. Patel, H. Park, Dynamics of tension leg platform tethers at low tension. part i - mathieu stability at large parameters, Marine Structures 4 (3) (1991) 257–273 (jan 1991). doi:10.1016/0951-8339(91)90004-u.

[9] A. N. Simos, C. P. Pesce, Mathieu stability in the dynamics of tlp's tethers considering variable tension along the length, in: Transactions on the Built Environment, vol. 29, 1997 (1997).

[10] I. K. Chatjigeorgiou, S. A. Mavrakos, Bounded and unbounded coupled transverse response of parametric excited vertical marine risers and tensioned cable legs for marine applications, Applied Ocean Research 24 (2002) 341–354 (2002).

[11] I. Chatjigeorgiou, On the parametric excitation of vertical elastic slender structures and the effect of damping in marine applications, Applied Ocean Research 26 (1-2) (2004) 23–33 (feb 2004). doi:10.1016/j.apor.2004.08.001.

[12] I. K. Chatjigeorgiou, S. A. Mavrakos, Nonlinear resonances of parametrically excited risers - numerical and analytic investigation for $\Omega = 2\omega_1$, Computers & Structures 83 (8) (2005) 560 – 573 (2005). doi:10.1016/j.compstruc.2004.11.009.
URL http://www.sciencedirect.com/science/article/pii/S0045794904004602

[13] C. E. N. Mazzilli, Effect of linearly varying normal force upon the nonlinear modal analysis of slender beams, in: Proceedings of the 6th European Nonlinear Dynamics Conference - ENOC2008, 2008 (2008).

[14] X. Zeng, W. Xu, X. Li, Y. Wu, Nonlinear dynamic responses of the tensioned tether under parametric excitations, in: Proceedings of the 18th International Offshore and Polar Engineering Conference, ISOPE2008 (2008).

[15] H. Yang, F. Xiao, P. Xu, Parametric instability prediction in a top-tensioned riser in irregular waves, Ocean Engineering 70 (2013) 39–50 (sep 2013). doi:10.1016/j.oceaneng.2013.05.002.

[16] H. Yang, F. Xiao, Instability analyses of a top-tensioned riser under combined vortex and multi-frequency parametric excitations, Ocean Engineering 81 (2014) 12–28 (may 2014). doi:10.1016/j.oceaneng.2014.02.006.

[17] G. Franzini, C. Pesce, R. Gonçalves, A. Fujarra, P. Mendes, An experimental investigation on concomitant vortex-induced vibration and axial top-motion

550    excitation with a long flexible cylinder in vertical configuration, Ocean Engi-
       neering 156 (2018) 596–612 (may 2018). `doi:10.1016/j.oceaneng.2018.`
       `02.063.`

[18]   C. E. N. Mazzilli, S. Lenci, L. Demeio, Non-linear free vibrations of tensioned
       vertical risers, in: Proceedings of the 8th European Nonlinear Dynamics Con-
555    ference - ENOC2014, 2014 (2014).

[19]   I. Senjanović, A. M. Ljuština, J. Parunov, Natural vibration analysis of tensioned
       risers by segmentation method, Oil & Gas Science Technology 61 (2006) 647–
       659 (2006). `doi:http://dx.doi.org/10.2516/ogst:2006004.`

[20]   I. K. Chatjigeorgiou, Solution of the boundary layer problem for calculating the
560    natural modes of riser-type slender structures, Journal of Offshore Mechanics
       and Arctic Engineering 130 (2008) 011003–011003–7 (2008).

[21]   S. Chandrasekaran, N. Chandak, G. Anupam, Stability analysis of TLP theters,
       Ocean Engineering 33 (2006) 471–482 (2006).

[22]   M. Keber, M. Wiercigroch, Comparison of dynamical responses of an offshore
565    riser with linear and nonlinear structural characteristics through nonlinear
       normal modes, in: OCEANS 2007 - Europe, IEEE, 2007 (jun 2007). `doi:`
       `10.1109/oceanse.2007.4302410.`

[23]   M. Keber, M. Wiercigroch, Dynamics of a vertical riser with weak structural
       nonlinearity excited by wakes, Journal of Sound and Vibration 315 (3) (2008)
570    685–699 (aug 2008). `doi:10.1016/j.jsv.2008.03.023.`

[24]   S. W. Shaw, C. Pierre, Normal modes for non-linear vibratory systems, Journal
       of Sound and Vibration 164 (1993) 85–124 (1993).

[25]   G. R. Franzini, C. C. P. Santos, C. E. N. Mazzilli, C. P. Pesce, Parametric excita-
       tion of an immersed, vertical and slender beam using reduced-order models:
575    influence of hydrodynamic coefficients, Marine Systems & Ocean Technology
       11 (1-2) (2016) 10–18 (apr 2016). `doi:10.1007/s40868-016-0013-z.`

[26]   G. R. Franzini, T. Dias, C. Mazzilli, C. P. Pesce, Parametric excitation of an
       offshore riser using reduced-order models based on bessel-type modes: as-
       sessment on hydrodynamic coefficients effects, in: Proceedings of the 6th

580      International Conference on Nonlinear Science and Complexity, INPE In-
stituto Nacional de Pesquisas Espaciais, 2016 (2016). `doi:10.20906/cps/`
`nsc2016-0009`.

[27] C. E. N. Mazzilli, T. Dias, Non-linear reduced-order modelling of heave-
imposed motion in vertical risers, in: Proceedings of the 15th Pan-American
585      Congress of Applied Mechanics - PACAM XV, 2015 (2015).

[28] C. E. Mazzilli, F. Rizza, T. Dias, Heave-imposed motion in vertical risers: A
reduced-order modelling based on bessel-like modes, Procedia IUTAM 19
(2016) 136–143 (2016). `doi:10.1016/j.piutam.2016.03.018`.

[29] G. R. Franzini, A. Gay Neto, Numerical investigations on parametric excitation
590      of a vertical beam under prescribed axial displacements, in: Proceedings of the
22nd International Conference on Sound and Vibration, 2015 (2015).

[30] G. R. Franzini, C. E. N. Mazzilli, Non-linear reduced-order model for parametric
excitation of vertical and immersed slender rod, International Journal of Non-
linear Mechanics 80 (2016) 29–39 (2016). `doi:10.1016/j.ijnonlinmec.`
595      `2015.09.019`.

[31] C. E. N. Mazzilli, C. T. Sanches, O. G. P. Baracho Neto, M. Wiercigroch, M. Ke-
ber, Non-linear modal analysis for beams subjected to axial loads: Analytical
and finite-element solutions, International Journal of Non-linear Mechanics 43
(2008) 551–561 (2008). `doi:10.1016/j.ijnonlinmec.2008.04.004`.

600 [32] A. H. Nayfeh, B. Balachandran, Applied Nonlinear Dynamics: Analytical, Com-
putational and Experimental Methods, John Wiley & Sons, Inc., 1995 (1995).

[33] C. Sparks, Transverse modal vibrations of vertical tensioned risers. a simplified
analytical approach, Oil & Gas Science and Technology 57 (1) (2002) 71–86 (jan
2002). `doi:10.2516/ogst:2002005`.

605 [34] A. G. Neto, C. A. Martins, P. M. Pimenta, Static analysis of offshore risers
with a geometrically-exact 3d beam model subjected to unilateral contact,
Computational Mechanics 53 (1) (2013) 125–145 (jul 2013). `doi:10.1007/`
`s00466-013-0897-9`.

[35] A. G. Neto, Dynamics of offshore risers using a geometrically-exact beam model with hydrodynamic loads and contact with the seabed, Engineering Structures 125 (2016) 438–454 (oct 2016). `doi:10.1016/j.engstruct.2016.07.005`.

[36] A. G. Neto, Giraffe user's manual - generic interface readily accessible for finite elements, http://sites.poli.usp.br/p/alfredo.gay/, accessed 25 Jan 2019 (2019).

610